International Journal of Heat and Mass Transfer 88 (2015) 111–121

Contents lists available at ScienceDirect

International Journal of Heat and Mass Transfer

journal homepage: www.elsevier.com/locate/ijhmt

# Microscale study of mechanisms of heat transfer during flow boiling in a microchannel

Sajjad Bigham, Saeed Moghaddam *

*Department of Mechanical and Aerospace Engineering, University of Florida, Gainesville, FL 32611, United States*

ARTICLE INFO

*Article history:*
Received 30 December 2014
Received in revised form 8 April 2015
Accepted 13 April 2015
Available online 14 May 2015

*Keywords:*
Flow boiling
Microchannel
Microlayer evaporation
Transient conduction

ABSTRACT

This study examines the microscale physics of heat transfer events in flow boiling of FC-72 in a microchannel. Experimental results presented here provide new physical insight on the nature of heat transfer processes during bubbles growth and flow through the microchannel. The study is enabled through development of a device with a composite heated wall that consists of a high thermal conductivity substrate coated by a thin layer of a low thermal conductivity material with embedded temperature sensors. This novel arrangement enables calculation of the local heat flux with a spatial resolution of 40–65 μm and a temporal resolution of 50 μs. The device generates isolated bubbles from a 300 nm in diameter artificial cavity fabricated at the center of a pulsed function micro-heater. Analysis of the temperature and heat flux data along with synchronized images of bubbles show that four mechanisms of heat transfer are active as a bubble grows and flows through the channel. These mechanisms of heat transfer are (1) microlayer evaporation, (2) interline evaporation, (3) transient conduction, and (4) micro-convection. Details of these mechanisms including their time period of activation and corresponding surface heat flux and heat transfer coefficient are extensively discussed.

Published by Elsevier Ltd.

## 1. Introduction

Flow boiling is a prominent mechanism of heat transfer in numerous applications ranging from small-scale refrigeration systems used in most buildings [1–4] to power plant boilers. The need for heat removal from confined spaces in modern applications has generated significant interest in implementing flow boiling in channels that are an order of magnitude smaller than the large tubes used in traditional boiling applications (i.e. microchannels) [5,6]. Examples of such applications are high performance CPUs, X-band radars, and power electronics [7–9] in which fabrication of high density integrated circuits has led to an ever-increasing generation of waste heat that hinders development/deployment of enhanced electronics systems.

Although flow boiling in microchannels has been studied for decades [10–18], its physical nature is still plagued with significant uncertainties. A large part of this uncertainty stems from the complex coupling of mass, momentum, and energy transport that occurs between different phases. This complexity in the flow and energy fields, and the lack of physical understanding of the processes, have arisen different and often contradictory hypotheses [19–27] to describe the heat transfer events. Although great efforts have been devoted to the development of these models [17,23,28–30], their fundamental assumptions have not been examined due to the lack of necessary tools to probe the actual physics of the proposed mechanisms. These models are often constructed based on observations of the overall trends in flow thermohydraulics characteristics as a function of externally controlled parameters (i.e. flow rate, heat flux, surface temperature, and fluid properties) as well as the observed flow regimes. The performance of the models has often been evaluated based on their ability to predict the overall surface heat transfer coefficient, which is the cumulative effect of all micro-scale sub-processes of boiling.

Therefore, new measurement tools are required to decipher the physical nature of heat transfer events in flow boiling in microchannels. Perhaps, the first step in enhancing our understanding of the heat transfer mechanisms is to analyze the thermal field around a bubble during its growth and flow through the channel. One of the main challenges in achieving this objective is implementation of adequate measurement tools [31] for resolving the surface heat flux at a sufficiently high spatial and temporal resolution. In light of significant advancements in microfabrication capabilities, a few attempts have been made to achieve this objective [32–34]; however, accurate accounts of the local surface heat flux and the heat transfer coefficient and their variations are not

* Corresponding author.
*E-mail address:* saeedmog@ufl.edu (S. Moghaddam).

http://dx.doi.org/10.1016/j.ijheatmasstransfer.2015.04.034
0017-9310/Published by Elsevier Ltd.

presented. The difficulty arises from the fact that different heat transfer mechanisms are coupled through heat conduction within the substrate [32,35] and the account of heat transfer due to one mechanism is not possible without making assumptions regarding the heat transfer events taking place at neighboring regions.

This study presents a novel platform for accurate resolution of the thermal field at the wall and bubble interface. In the following sections, first, main challenges associated with measurement of the local heat flux are discussed and the measurement approach implemented here is subsequently introduced. The new approach is then utilized to resolve the surface temperature and heat flux at an unprecedented spatial and temporal resolution. The magnitude and activation time period of different heat transfer mechanisms are discussed in details. Finally, the similarities observed in the underlying heat transfer mechanisms of the nucleate pool boiling and the microchannel flow boiling processes are discussed.

## 2. Heat flux measurement challenges and a new approach

The main challenge in resolving the thermal field at the solid–fluid interface is the measurement of the surface heat flux. Heat flux at the interface rapidly changes due to spatial and temporal variations of the boundary conditions. The variations are due to the bubbles nucleation, expansion, and movements along the channel, which result in the formation and evaporation of thin liquid films with varying thickness, contact line movements, and rapid surface wetting and dryout. On a typical boiling surface, significant heat flow within the solid occurs, which mirrors changes in the boundary conditions. For example, when a portion of the surface dries out, the local surface heat flux approaches zero and heat rushes to neighboring areas that might be experiencing a different boundary condition – potentially, one with an extremely high heat transfer coefficient, such as evaporation of a very thin liquid film or a surface rewetting event. This explanation clearly highlights the fact that the actual heat flux at the solid-fluid interface can never be constant. As will be shown later in this paper, heat flux can change from zero to its maximum within less than 100 μs and regions with maximum and minimum (near zero) heat flux could be only a few micrometers apart.

In the absence of a viable approach for accurate measurement of the surface heat flux, different strategies have been implemented to determine the surface heat flux. Attempts have been made to subject the heated surface to a constant heat flux [36], numerically calculate the surface flux by solving the thermal field within the solid using experimental surface temperature data [35,37,38], and electronically varying the heat flux across a micro-heater array such that the surface temperature always remains constant [39]. To set the stage for the introduction of the new approach proposed in this study, these three fundamentally different approaches are discussed below.

Zhang et al. [36] study could be considered the first attempt on the microscale instrumentation of two-phase flow microchannels. To understand the process physics and model heat transfer, Zhang et al. [36] conducted experimental studies on boiling water in microchannels with hydraulic diameters between 25 and 60 μm. Zhang et al. [36] thinned down the microchannel heated wall and built it on a bridge structure to minimize heat loss and to provide "a nearly constant heat flux boundary condition". The heating medium was a single thin film resistor and the temperature was measured using thin film temperature sensors. The study produced temperature variations along the channel length at different heat inputs. However, it did not provide any high-resolution data indicative of the presence as well as magnitude of the boiling sub-processes and their relative contributions to the overall surface heat transfer.

Wagner and Stephan [37] used an infrared camera to measure temperature distribution on the backside of a 20-μm-thick stainless steel heating foil during boiling of FC-84 and FC-3284. The temperature recording was synchronized with a camera capturing bubbles images. The temperature data was recorded at a frequency of 978 Hz and the bubbles images were captured at a rate of 1000 frames/s. The local heat flux was obtained by performing an energy balance for each pixel by estimating the sensible heating, heat generation and lateral conduction within the foil, and heat loss to the fluid. The total latent heat transferred into the bubble was calculated from changes in the bubble volume between time steps. Using these data, Wagner and Stephan [39] concluded that heat transfer predominately takes place at the bubble and surface contact line.

In a fundamentally similar approach to that of Wagner and Stephan [37], Yabuki and Nakabeppu [35] investigated the heat transfer mechanism under an isolated bubble during the nucleate boiling of water. They utilized a numerical model to calculate the surface heat flux. However, they used silicon as their substrate (cf. Fig. 1a) and micro-fabricated thermocouples to measure the surface temperature. Heat was supplied to the fluid by a thin film heater fabricated on the substrate and it was electrically isolated from the thermocouples using a 2-μm-thick silicon oxide layer. The temperature data was recorded at a sampling rate of 100 kHz and the bubbles images were recorded at a rate of 4000 frames/s. Their data indicated a drop in surface temperature at the bubble-surface contact area during the bubble growth due to the evaporation of a thin liquid layer formed beneath the bubble. After a short period of temperature rise, the surface cooled again. The authors argued that the subsequent surface temperature drop is due to another neighboring cooling event that impacted (through lateral heat conduction within the substrate) the temperature rise of an otherwise dried-out surface. Using the measured temperature data, the authors computed the local heat flux through a simulation of transient heat conduction within the substrate.

Yabuki and Nakabeppu's [35] observation of the impact of one heat transfer event on another clearly demonstrates the fact that the substrate couples different heat transfer mechanisms that are simultaneously active on a boiling surface. One might assume that lowering the substrate conductivity and significantly reducing its thickness could resolve this issue. But, in fact, if Yabuki and Nakabeppu's [35] had used an extremely thin low-conductivity substrate to eliminate the lateral heat conduction (i.e. provide a constant heat flux boundary condition), the substrate temperature would have greatly increased at the dried out spot because heat would have not been able to enter the fluid nor it could have spread through the substrate. Evidently, Rao et al.'s [32] use of a low thermal conductivity but thick substrate resulted in temperature spikes as high as 150 °C at the dried out site.

These facts highlight an interesting dilemma: on a typical surface, the boiling sub-processes are coupled through the substrate but we would like to decouple them to study their details. In an effort to decouple heat transfer in the two domains (i.e. solid and fluid), several years prior to Yabuki and Nakabeppu's study [35], Demiray and Kim [39] used a microheater array consisting of 96 independently controlled heaters each nominally $0.1 \times 0.1\ mm^2$ in size to measure the surface heat flux distribution underneath the bubbles. The microheaters were also used to measure the surface temperature, which was kept constant through the use of analog electronic feedback circuits that controlled power input to the heaters. Demiray and Kim [39] used a quartz substrate, but the constant temperature maintained over the surface eliminated the coupling. The quartz substrate was merely used to minimize the heat loss from the microheaters' array area to the non-heated neighboring areas that were also impacted by the convective

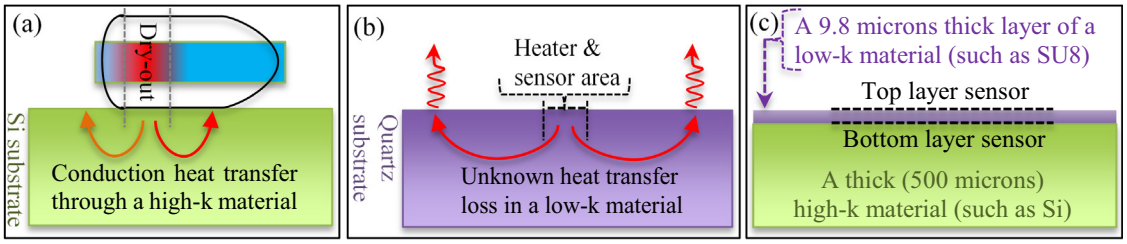


**Fig. 1.** Schematics of (a) conduction heat transfer in high-k material, (b) unknown heat transfer losses in low-k material, and (c) a composite wall with embedded sensors.

currents generated due to boiling. Demiray and Kim [39] used FC-72 as the test fluid. The heaters power input was resolved at a frequency of 2–3 kHz and the bubbles images were captured at a rate of 3704 frames/s. The heaters array put out a significant amount of heat at a relatively constant rate. The results showed sudden rises in heat output correspond to individual nucleation events. Demiray and Kim [39] filtered out the near steady heat flux portion of the total heat transfer to determine the heat flux corresponding to an individual bubbling event.

The Demiray and Kim's [39] data clearly showed that the bubble heat transfer events are responsible for a small fraction of the total heater array power. Therefore, throwing away the unaccounted heat transfer rates risks eliminating heat transfer events that could have a rather steady nature. Attempts have been made to account for the amount of heat spread through the substrate beyond the heater array region (i.e. heat loss). However, some assumptions must be made to determine the surface heat flux (cf. Fig. 1b). For example, in an effort by the same group, Myers et al. [40] assumed that the heat transfer regime outside their $1 \times 1$ mm$^2$ microheater array (fabricated on a 0.5-mm-thick quartz substrate) is governed by natural convection, with a heat transfer coefficient of 200 W/m$^2$ K. Using this boundary condition for outside the microheater array area and the experimental temperature data on the microheater array, they numerically estimated the surface to fluid heat flux. Moghaddam [41] conducted a comprehensive analysis of the substrate heat loss and concluded that different assumptions for thermal boundary conditions outside the array area can result in vastly different values for heat flux within the array area. It was shown that the substrate heat loss could be several times greater than the surface to liquid heat flux at the array area, even when quartz is used as the substrate.

To avoid the challenges discussed in the previous measurement studies, Moghaddam and Kiger [42,43] developed a method for local measurement of the surface heat flux. To overcome shortcomings inherent to using a monolithic low-conductivity wall, Moghaddam and Kiger [42,43] designed a device with a composite wall consisting of a highly conductive wall, such as silicon, covered with a coating (10 μm thick) of a low thermal conductivity polymer (cf. Fig. 1c). In boiling dielectric liquids (e.g. FC-72), the silicon wall remains at a relatively constant temperature thus providing a constant surface temperature boundary condition at the silicon-polymer interface during the nucleation process, owing to the relatively high thermal conductivity of silicon. Under these conditions, any change in the surface heat flux directly changes the temperature at the top of the polymer layer. A steady-state temperature difference between the solid-fluid interface and the polymer-silicon interface multiplied by the polymer conductivity is a measure of heat flux. Also, since the polymer layer has a low thermal conductivity, lateral heat conduction within the polymer layer is low. As a result, for example, a several microns wide heat flux sensor made of a micron thick polymer can measure the heat flux without much crosstalk with its neighboring sensor. However, when the heat conduction equation within the polymer layer is numerically solved to determine the surface heat flux, only the size of the smallest manufacturable temperature sensor limits the minimum size of the area over which the surface heat flux can be determined. Details of a device fabricated based on this measurement method is discussed in the following section.

## 3. Test article

A schematic of the experimental device and a detailed view of the microfluidic chip are shown in Fig. 2. The device consists of a single rectangular microchannel with inlet and outlet ports for fluid entry and exit. The microchannel wall is made of a 75 μm-thick SU8 film and is sealed by a Polydimethylsiloxane (PDMS) transparent cap. The microchannel width is 300 μm. After the inlet port, there is a pre-heater section in which the working fluid, FC-72, is heated up to the desired temperature before entering the test section. The microfluidic chip is fabricated on a silicon wafer through a multistep microfabrication process.

As shown in Fig. 2, the bottom surface of the test channel is a composite wall made of a thick high thermal conductivity (high-k) material (a 500 μm thick silicon substrate) coated with a low-conductivity (low-k) film (a 9.8 μm thick layer of SU8). A total of 53 platinum resistance temperature detectors (RTD) are sputter deposited at the fluid-SU8 and SU8-silicon interfaces to measure the temperature distribution during the boiling process. The thickness of the sputtered platinum layer is 120 nm. Several thin film heaters are also embedded at the SU8-silicon interface. The sensors and the heaters have a 50-nm-thick titanium adhesion layer and gold bond pads. The RTD sensors are 50 μm wide and are placed 15 μm apart in the flow direction.

To control the nucleation site, a 300 nm in diameter cavity is fabricated using a focused ion beam (FIB) milling machine. The cavity is surrounded by a pulsed function microheater fabricated on the SU8 film. A SEM image of the artificial cavity and the pulsed function microheater is shown in Fig. 3. Changing the amplitude and period of the pulsed function microheater subjects the liquid immediately adjacent to the cavity at different metastable superheated conditions (i.e. non-equilibrium thermodynamic conditions) [44]. As a result, the liquid undergoes phase change generating different flow regimes based on the characteristic of the applied pulsed function. To increase the accuracy of the temperature measurements, a 4-wire configuration, also referred to as Kelvin connection, is utilized. The 4-wire configuration uses one pair of wires to deliver the excitation current (Ex. +/−) to the RTD sensor and uses a separate pair of wires to sense the voltage across the sensor (Ch. +/−) (cf. Fig. 4). Because of the high input impedance of the differential amplifier, negligible current flows through the sense wires. This results in a very small voltage drop error due to the lead resistance [45].

## 4. Experimental apparatus

The microfluidic chip is wire bonded to a custom made double sided printed circuit board (PCB), as shown in Fig. 5c. Since each

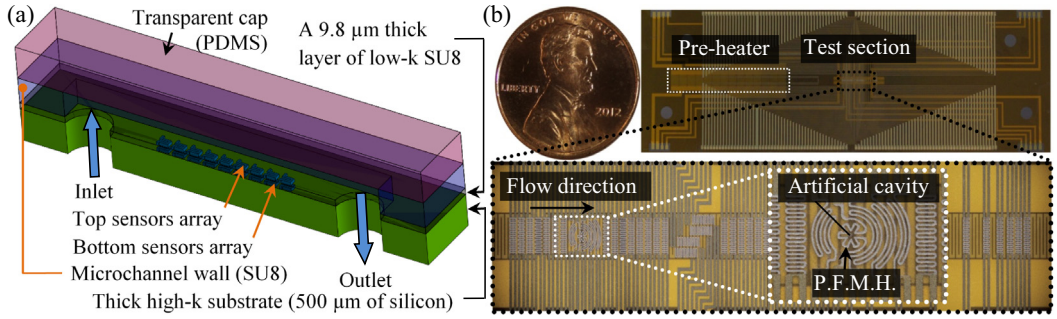


**Fig. 2.** (a) A schematic of the experimental device, (b) a detailed view of the microfluidic chip (test section, pre-heater, artificial cavity and pulsed function microheater (P.F.M.H.) are labeled.).

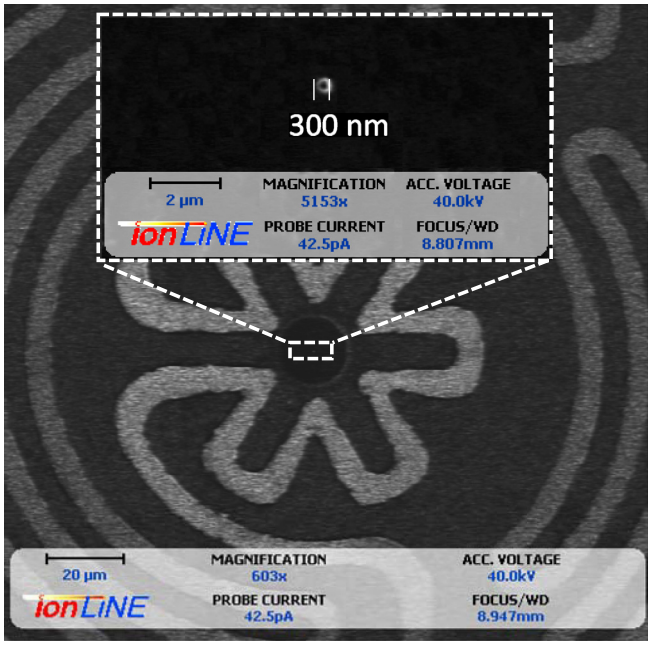


**Fig. 3.** A SEM image of a 300 nm cavity fabricated by FIB at the center of the pulsed function microheater.

RTD sensor has four connections (excitation +/− and channel amplifier +/−) (cf. Fig. 4), all similar connections from all sensors are guided to a separate 50-pin ribbon socket to be electrically connected to a data acquisition (DAQ) system. The DAQ system which consists of a current excitation module (NI SCXI-1581), a channel amplifier module (i.e. signal conditioning module) (NI SCXI-1120C), a high speed DAQ module (NI PXI-6289) and a programmable dc power supply module (NI PXI-4110) is commanded by an embedded controller (NI PXI-8115). The temperature data are recorded at a frequency of 20 kHz. The pulsed function microheater is physically connected to the programmable dc power supply module. All data collections as well as controlling the applied dc voltage to the pulsed function microheater are performed in a single LabVIEW program. The thin film heaters are also powered by the NI PXI-4110 dc power supply. A high-speed camera (FASTCAM SA4-Photron) is synchronized with the DAQ to visualize the boiling process at a frequency of 20 k frames/s.

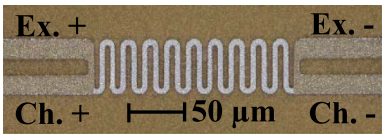


**Fig. 4.** A close view of a RTD sensor with the Kelvin connection.

Fig. 5a shows a schematic of the experimental setup designed to conduct the flow boiling experiments. The working fluid is delivered to the microfluidic chip by a piezoelectric micropump (Model MP6, manufactured by Bartels Mikrotechnik GmbH). Two PX-26 pressure transducers with ±1% reading error are used to measure the pressure drop across the microchannel. The working fluid is degassed by vigorous boiling for several hours before each experiment. Then, the desired surface temperature is adjusted and allowed about 15 min to reach steady state before recording the data.

## 5. Sensors calibration and uncertainty analysis

The RTD sensors are calibrated prior to the flow boiling experiments to obtain the voltage-temperature relationship of each sensor. The calibration tests are done in a uniform temperature oven for a temperature range of 40–90 °C. A constant current excitation of 100 μA is supplied to each sensor. Temperature sensors have a negligible self-heating. The obtained voltage-temperature curves show a linear trend and the sensitivity of the RTD sensors (the slope of the $V$–$T$ curves) is 0.13 mV/°C. The data acquisition system has a maximum uncertainty of ±28 μV at a gain of 100 with a minimum detectable voltage change of 1 μV. Table 1 provides the overall uncertainty of different variables.

## 6. Results and discussions

As mentioned previously, to generate different flow regimes under more controlled conditions, the device is equipped with a single cavity at the center of a pulsed function microheater. The cavity provides the vapor embryo for a heterogeneous bubble nucleation and the microheater converts the liquid surrounding the cavity to different metastable conditions [44]. The applied voltage to the microheater is a periodic square pulse. Since the total surface covered by the microheater is quite small (~0.004 $mm^2$), the heater supplies a negligible amount of heat to the liquid. A demonstration of different generated flow regimes is shown in Fig. 6. When the applied pulsed voltage is small (an amplitude of about 0.1–0.2 V), a bubbly flow regime downstream of the cavity is generated (cf. Fig. 6a). By increasing the strength and time period of the applied voltage to higher values (an amplitude of about 0.3–0.4 V), bubbly flow regime turns to a slug flow regime (cf. Fig. 6b). The annular flow regime is achieved when the applied pulse voltage has an amplitude of about 0.5–0.6 V and the surface temperature downstream of the cavity increases well above the saturation temperature (cf. Fig. 6c).

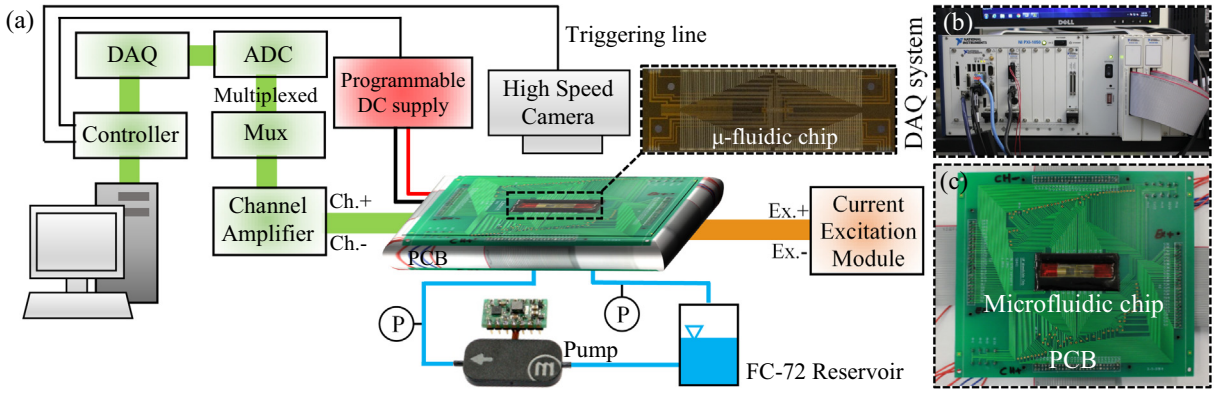


**Fig. 5.** (a) A schematic of the experimental setup, (b) an image of DAQ system, (c) microfluidic chip wire bonded to a custom made PCB (components are not to scale).

**Table 1**
Variables uncertainties.

| Variable | Uncertainty |
|---|---|
| Temperature | 0.2 °C |
| SU8 film thickness | 0.01 μm |
| Local heat flux | 0.7 W/cm$^2$ |

In the following section, wall heat transfer mechanisms associated with the flow of an isolated bubble passing over the sensor array is comprehensively investigated at a test flow rate of 3.3 mL/hr (i.e. a mass flux of 68.4 kg/m$^2$ s).

### 6.1. Analysis of the local temperature data

Fig. 7 shows the images of a moving elongated bubble during its growth in the microchannel. Fig. 8 shows the corresponding surface temperature data at different locations (sensors 26–28) as well as the average temperature of the sensors embedded at the SU8-Silicon interface. The temperature–time histories are presented starting from an arbitrary time before the arrival of the vapor bubble to sensor 26 (S26). At this time, the temperatures at the fluid-SU8 and the SU8-silicon interfaces are almost 61.7 and 62.5 °C, respectively. The temperature variations start by a drop in the surface temperature of S26 at $t = 1$ ms and progress over the subsequent sensors after about 50–150 μs. Comparison of the bubble images with the corresponding temperature data shows that the temperature drop starts after the front side of the moving bubble arrives at each sensor footprint (frames A and B). Therefore, the observed temperature drop is due to phase change cooling resulting from microlayer and/or interline evaporation modes of heat transfer. As the bubble moves over the sensor footprints, the sensors temperature continue their decreasing trends down to about 58.5 °C (frame C and corresponding temperature data). After a while, the surface temperature starts increasing ($t = 6$–$9$ ms). The reason for this temperature rise is that, as the bubble grows in size, it becomes more difficult to replenish the evaporated liquid, thus resulting in a shortage of the available liquid for phase change heat transfer. This shortage becomes more evident if one compares images of C and D in Fig. 7. After this step, the sensor temperatures remain at a fairly high temperature with a slight slope in their values towards the average temperature measured at the SU8-Silicon interface. The comparison of the temperature data with the bubble images also reveals that the surface temperature rapidly decreases when the rear side of the moving bubble passes the sensor footprints (frame E). At the end, once the bubble completely passes a sensor, the sensor temperature recovers to that of the single-phase flow condition.

To determine whether the observed temperature drop of the sensors is due to the evaporation of the microlayer formed on the surface or that of the apparent interline region seen as a dark shadow in the images, the temperature data of sensors 21–24 are examined. Unlike S26–28, these sensors are aligned parallel to the flow. Fig. 9 shows an image of the moving bubble over these sensors at $t = 8.3$ ms as well as their temperature data. As it can be seen, the apparent interline is on S21 and S24 while S22 and S23 do not have an apparent interline associated with them. As shown, for the examined thermal condition, no significant difference in the temperature data of S21 and S24 (with only microlayer evaporation mode of heat transfer) and S22 and S23 (with mixed microlayer and interline evaporation modes of heat transfer) is observed.

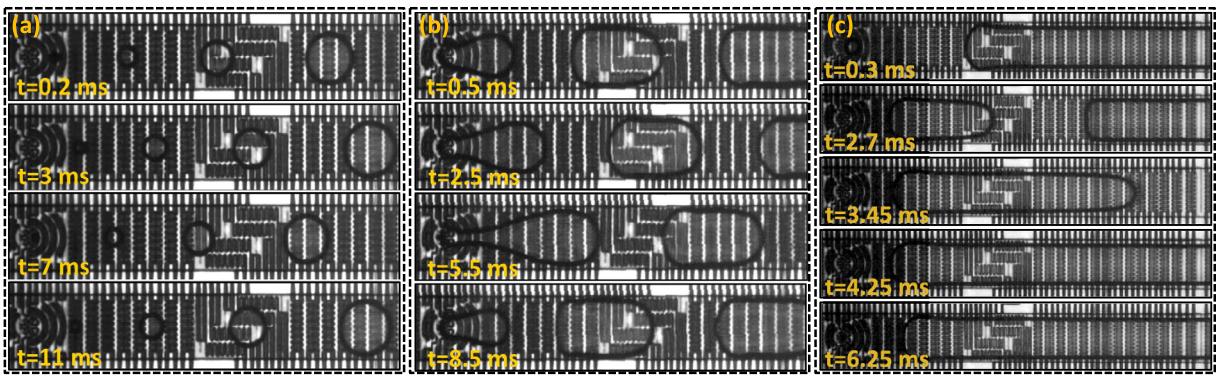


**Fig. 6.** Different flow regimes generated by the device; (a) bubbly flow regime, (b) slug flow regime, and (c) annular flow regime.

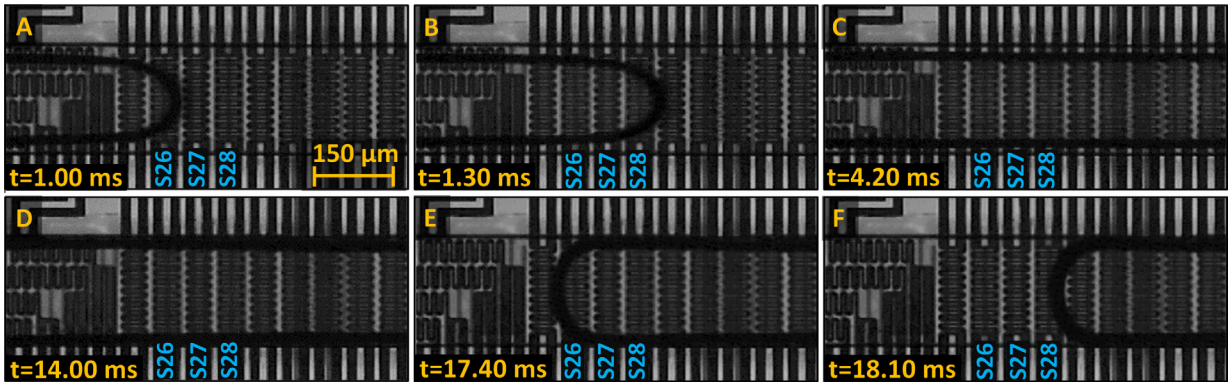


**Fig. 7.** Images of a moving elongated bubble during its growth due to evaporation (Ave. Temp. at SU8-Si interface = 62.5 °C).

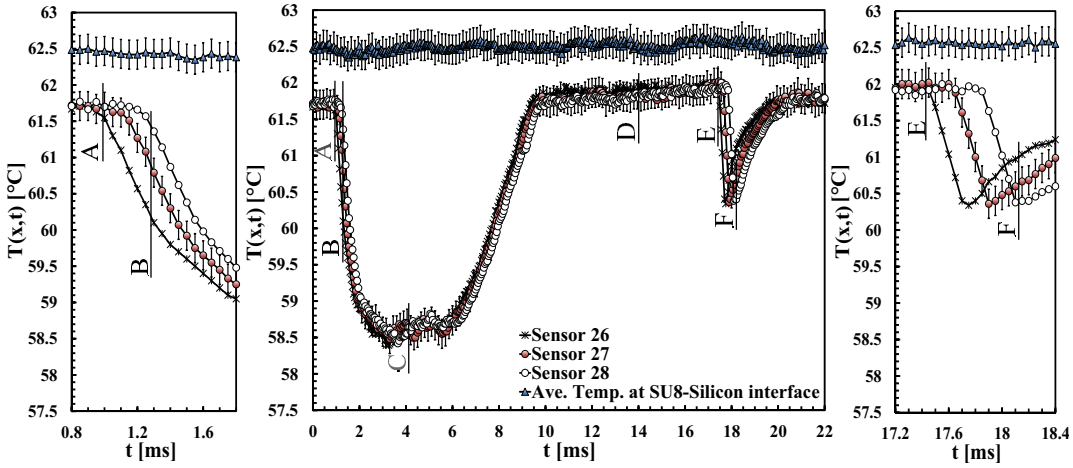


**Fig. 8.** Temperature–time histories measured at S26-28 (Ave. Temp. at SU8-Si interface = 62.5 °C).

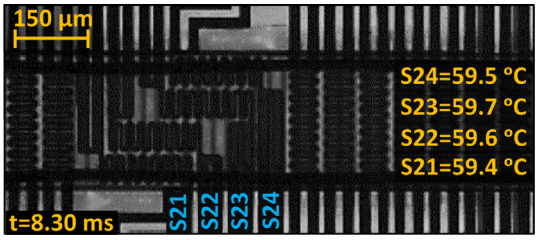


**Fig. 9.** Bubble image and corresponding temperature data of S21-S24 at $t$ = 8.3 ms (Ave. Temp. at SU8-Si interface = 62.5 °C).

To better differentiate the microlayer and interline evaporation modes of heat transfer, a second test with a higher wall superheat temperature is conducted. Figs. 10 and 11 show the images and the corresponding temperature data of a moving elongated bubble at sensor locations S21 and S22. It should be noted that the measured temperature data of S23 and S24 are similar to those of S22 and S21, respectively. The average temperature at the SU8-Silicon interface is kept at 66 °C. The overall observed temperature trends of these sensors are similar to those of the first test. However, in this test, there is a distinct difference in the temperature data of S22 located at the middle of the channel (due to microlayer evaporation) and S21 positioned at the side of the microchannel (due to mixed microlayer and interline evaporation). Here, the temperature of S22 recovers earlier than S21 ($t$ = 4–6 ms for S22 compare to $t$ = 6–8 ms for S21). This means that the dryout first occurs at S22 and its temperature remains relatively higher than sensor 22 during the temperature recovery stage.

### 6.2. Analysis of local heat flux distribution

The local heat flux data are determined by solving a 2-D transient heat conduction equation within the 9.8 μm thick layer of low-k SU8. The temperature data of the embedded sensors at the SU8-fluid and SU8-silicon interfaces are used to specify the top and bottom temperature boundary conditions of the SU8 film (cf. Fig. 12). An adiabatic boundary condition is used for the two end sides of the SU8 layer (i.e., right and left edges of the computational domain). The thickness of the SU8 layer is 9.8 ± 0.01 μm. ANSYS Fluent software has been used to solve the transient heat conduction equation. Three uniform mesh sizes ranging from 0.1 to 0.5 μm are selected to examine the mesh independency of the simulation results. The results showed a negligible difference in the calculated heat flux (less than 0.3%) with successive mesh refinements. A zoomed view of the computational grid used for the simulation is shown in Fig. 12. The convergence criteria in each time step is the scaled residual of the energy equation becoming less than $10^{-15}$. At $t$ = 0, the temperature distribution within the SU8 layer is determined by solving the steady heat conduction equation with the mentioned boundary conditions. Fig. 12 which shows the initial temperature distribution of the low wall superheat test indicates a linear temperature profile within the SU8 layer at $t$ = 0. Once the initial temperature distribution is determined, the temperature of the top and bottom boundary conditions are updated based on the experimental data and subsequently the transient heat conduction equation is solved to determine the temperature distribution of the SU8 layer at $t$ = 50 μs. The procedures of

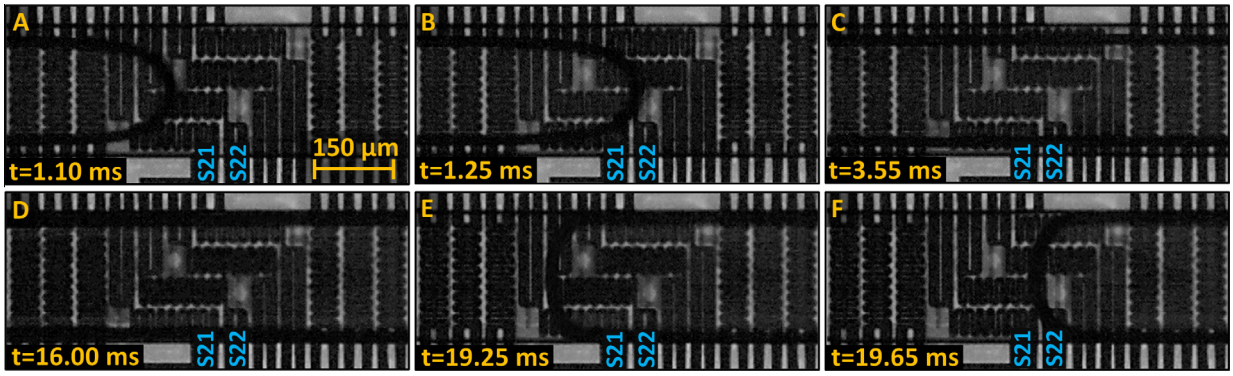


**Fig. 10.** Images of a moving elongated bubble during its growth due to evaporation (Ave. Temp. at SU8-Si interface = 66 °C).

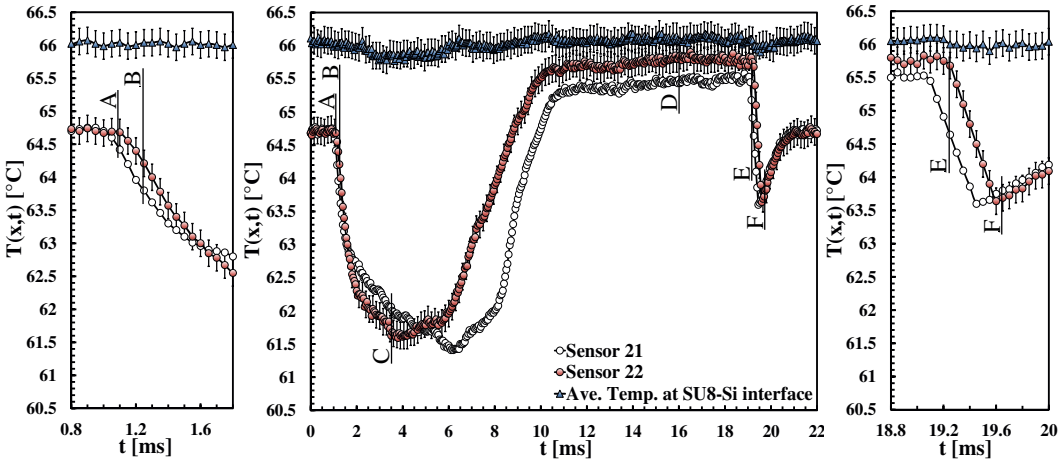


**Fig. 11.** Temperature–time histories measured at S21 and S22 (Ave. Temp. at SU8-Si interface = 66 °C).

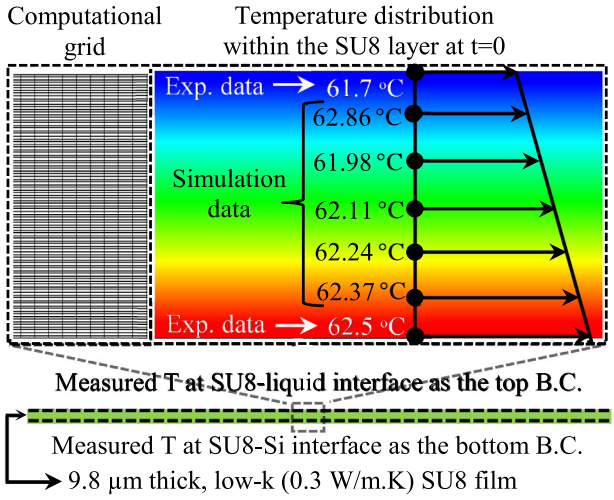


**Fig. 12.** Computational domain of the SU8 film.

updating the top and bottom boundary conditions and solving the transient heat conduction equation continues in time domain up to $t$ = 22 ms. The maximum uncertainty in the local heat flux data of the low and high wall superheat tests is estimated to be ±0.7 W/cm$^2$. The local uncertainty values of each data point are shown by an error bar in the heat flux curves.

The local heat transfer coefficients are then calculated based on the local temperature and heat flux data as follows:

$$h(x,t) = \frac{q''(x,t)}{T_{SU8-fluid}(x,t) - T_{sat}} \quad (1)$$

$T_{sat}$ is the saturation temperature of FC-72 at atmospheric pressure (56 °C). The maximum uncertainty in the two-phase to single-phase heat transfer coefficient ratio ($h_{T.Ph.}/h_{S.Ph.}$) is estimated to be ±1.

*6.2.1. Microlayer and interline evaporation heat transfer*

Fig. 13a presents the local heat flux data of sensor 27 as a function of time for the moving elongated bubble shown in Fig. 7 (i.e., the low wall superheat test). As it can be seen, the heat flux variations start by a heat flux spike up to about 11–13 W/cm$^2$. As expected from the temperature data, the sudden rise in the surface heat flux starts happening when the front side of the bubble reaches the sensor, which is indicative of the microlayer/interline evaporation mode of heat transfer. Following the initial heat flux spike, the local heat flux reaches a plateau with about 2 W/cm$^2$ heat flux variation. After a while, the local heat flux declines and reaches to a partial dry-out situation. The decreasing trend in the local heat flux can be explained upon examination of Fig. 7 (images C and D), where it can be observed that the liquid film located between the vapor region and the channel side walls is evaporated/disappeared. Therefore, a shortage of the available liquid phase results in gradual reduction in the local heat flux.

Fig. 13b representing the two-phase to single-phase heat transfer coefficient ratio ($h_{T.Ph.}/h_{S.Ph.}$) as a function of time indicates that the heat transfer coefficient of the two-phase flow is enhanced by about 14–16 times relative to that of the single-phase flow during the microlayer/interline evaporation mode of heat transfer. The

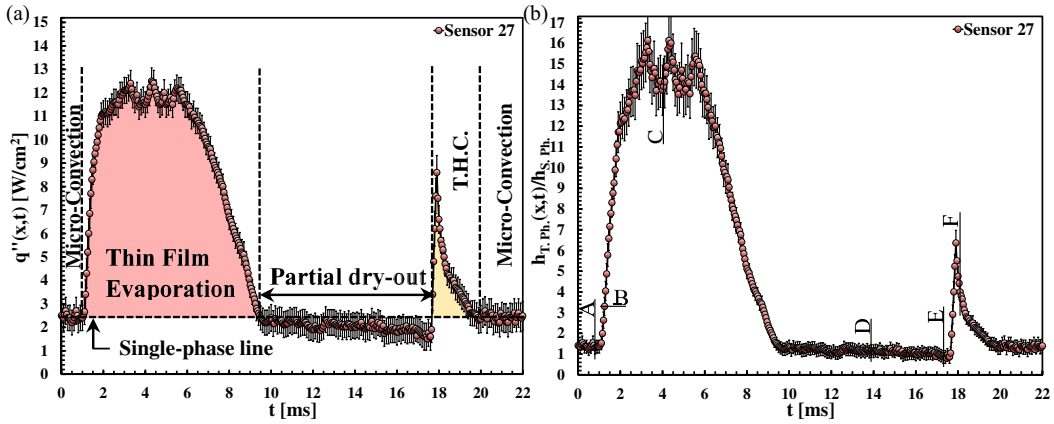


**Fig. 13.** (a) Local heat flux-time histories corresponding to temperature data of Fig. 8 measured at S27 and the respective heat transfer mechanisms associated with a moving elongated bubble during its growth due to evaporation in the microchannel, (b) two-phase to single-phase heat transfer ratio (corresponding to the temperature data of Fig. 8) as a function of time measured at S27.

single-phase heat transfer coefficient is calculated based on a single-phase flow test and is measured to be 3100 W/m$^2$ K (corresponding to a Nusselt number of 6.2).

Fig. 14a shows the local heat flux-time histories measured at S22 in the high wall superheat test. A similar heat transfer event (i.e., the microlayer/interline evaporation process) has been identified in this test once the bubble comes in contact with the sensor footprint (cf. images A, B and C in Fig. 10 and corresponding heat flux data in Fig. 14a). Fig. 14b illustrates that the two-phase heat transfer coefficient is enhanced by about 7–8 times compared to that of the single-phase flow during the microlayer/interline evaporation mode of heat transfer.

*6.2.2. Transient conduction and micro-convection heat transfer*

Comparison of the bubble images with the local heat flux data shows that towards the end of the partial dryout process, the local heat flux rapidly increases (cf. Figs. 13a and 14a) as the rear end of the bubble moves over, and rewets, the sensors (cf. Fig. 15a). After the liquid slug fully rewets the surface (cf. Fig. 15b), the local heat flux gradually decreases and reaches to a steady state condition. This sudden spike in the local heat flux during the rewetting process resembles observations made in pool boiling studies [39,42] during the bubble departure, as a liquid front advances over (i.e. rewets) the bubble-surface contact area after a dryout period following the microlayer evaporation process. This phenomenon arises from a mismatch between the surface and liquid temperatures as they come into contact. The physics of this process is consistent with what is commonly named as "transient conduction" mode of heat transfer that results from the rewetting of a hot surface with the cooler bulk liquid.

The transient conduction theory was initially utilized by Mikic and Rohsenow [46] to model surface heat flux during the pool boiling process. They assumed that a departing bubble pumps away the hot liquid from the surface and heat is transferred via transient conduction into the liquid that replaces the displaced fluid. They used the governing equation for heat transfer to a semi-infinite body [47] and derived the following equation for the surface heat flux:

$$q'' = f\int_0^{\frac{1}{f}} \frac{k_l \Delta T}{\sqrt{\pi \alpha_l t}}\,dt = \frac{2k_l \Delta T}{\sqrt{\pi \alpha_l t}}\sqrt{f} \tag{2}$$

Moghaddam and Kiger [48] showed that the transient conduction model of Mikic and Rohsenow [46] overpredicts the experimental results. They argued that the main reason for this difference is that unlike what is assumed in the Mikic and Rohsenow [46] model (i.e. sudden coverage of the entire surface with the bulk liquid), the surface rewetting process is gradual. During this process, the contact line rewets the surface with a finite velocity. So, the overall surface heat transfer is small before a significant part of the surface is

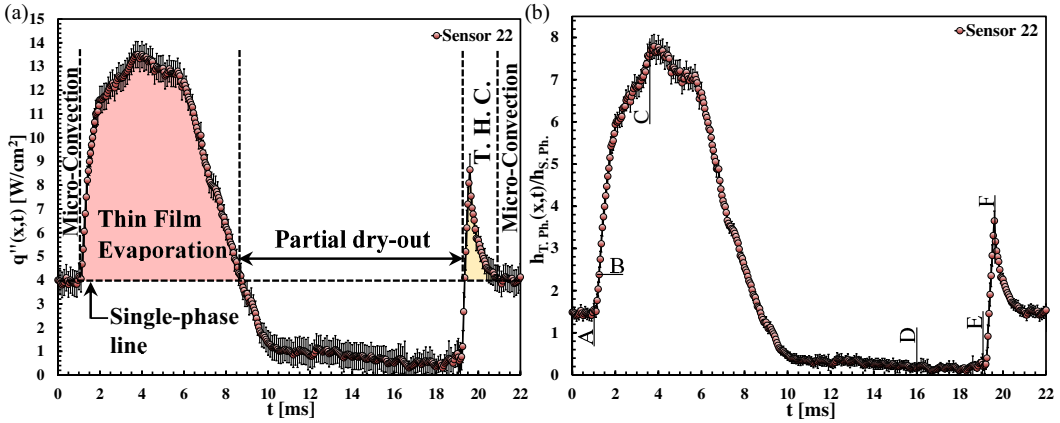


**Fig. 14.** (a) Local heat flux-time histories corresponding to the temperature data of Fig. 11 measured at S22 and the respective heat transfer mechanisms associated with a moving elongated bubble during its growth due to evaporation in the microchannel, (b) two-phase to single-phase heat transfer ratio (corresponding to the temperature data of Fig. 11) as a function of time measured at S22.

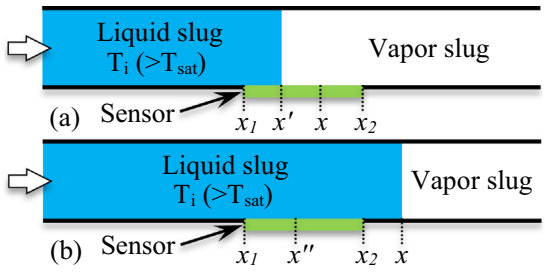


**Fig. 15.** Schematic of the advancing liquid front on the heat transfer surface.

covered with the liquid [48]. Demiray and Kim [39] modified the transient conduction model to account for the gradual surface coverage. On the basis of the transient heat conduction model, during the gradual surface coverage, the surface heat flux can be determined by integrating the governing equation for the heat flux at an arbitrary point $x'$ when the sensor is covered with the liquid front at $t'$ (cf. Fig. 15a):

$$q_{TC}(t) = \int_{x_1}^{x} \frac{k\Delta T_{TC}}{\sqrt{\pi\alpha}} \frac{w}{\sqrt{t-t'}}\, dx' \tag{3}$$

Substituting $t = (x - x_1)/v$ and $t' = (x' - x_1)/v$ yields (the time origin is when the liquid front reaches point $x_1$):

$$q_{TC}(t) = \frac{k\Delta T_{TC} w\sqrt{v}}{\sqrt{\pi\alpha}} \int_{x_1}^{x} \frac{dx'}{\sqrt{x-x'}} \tag{4}$$

Transferring back to the time coordinate results:

$$q_{TC}(t) = \frac{2k\Delta T_{TC} wv}{\sqrt{\pi\alpha}} \sqrt{t} \tag{5}$$

where $v$ is the velocity of the liquid front (obtained from experimental data), $w$ is the sensor width, $\Delta T_{TC}$ is the difference in the temperature of the surface and the rewetting liquid.

When the surface is completely rewetted (cf. Fig. 15b), the heat flux associated with the transient heat conduction model can be estimated by integrating the governing equation for heat flux at an arbitrary point $x''$ that has been in contact with liquid for $t - t'' = (x - x'')/v$.

$$q_{TC}(t) = \int_{x_1}^{x_2} \frac{k\Delta T_{TC}}{\sqrt{\pi\alpha}} \frac{w}{\sqrt{t-t''}}\, dx'' \tag{6}$$

Substituting $t = (x - x_1)/v$ and $t'' = (x'' - x_1)/v$ and transferring back to the time coordinate results:

$$q_{TC}(t) = \frac{2k\Delta T_{TC} wv}{\sqrt{\pi\alpha}} (\sqrt{t} - \sqrt{t-t_2}) \tag{7}$$

Eqs. (5) and (7) can be integrated and combined to determine the cumulative surface heat transfer.

$$Q_{TC}(t) = \begin{cases} \frac{4k\Delta T_{TC} wv}{3\sqrt{\pi\alpha}} t^{3/2} & \text{for } t \leqslant t_2 \\ \frac{4k\Delta T_{TC} wv}{3\sqrt{\pi\alpha}} (t^{3/2} - (t-t_2)^{3/2}) & \text{for } t > t_2 \end{cases} \tag{8}$$

A comparison between the cumulative heat transfer results (divided by the surface area of each sensor) from the experiment and those of the transient heat conduction model determined by Eq. (8) is presented in Fig. 16. The comparison shows a relatively close match between the two with $\Delta T_{TC} = 0.45\Delta T$ in the case of low wall superheat test and $\Delta T_{TC} = 0.55\Delta T$ for the test conducted at high wall superheat. This agreement suggests that transient conduction heat transfer correlates well with the transient conduction theory when gradual surface coverage is taken into account. Intuitively, the difference in temperature of the rewetting liquid and the surface is lower than the surface superheat temperature.

The heat transfer event following the transient conduction process discussed above has an almost steady nature (the variations are within the experimental uncertainty of the heat flux), as seen in Figs. 13a and 14a. We refer to this mechanism the "micro-convection" heat transfer mode.

## 7. Comparison with nucleate pool boiling process

The heat transfer events associated with the microchannel flow boiling process have been hypothesized to have some similarities with those of the bubble ebullition process in pool boiling [49]. The differences between the two stem from differences in the dominant forces controlling the bubble dynamics and confinement effects. The gravitational forces, which are significant in the pool boiling process, have little impact on flow dynamics in microchannels where the inertia and surface tension forces are prominent. In spite of differences in governing force field, the interfacial interactions in both cases could result in similar thermal events, as mentioned by Kandlikar [49]. The microscale data provided in this study has provided an opportunity to examine this hypothesis in more details. The similarities and differences observed in the underlying heat transfer mechanisms are highlighted below.

1. In the pool boiling process, once a bubble nucleates and expands over the surface, it forms a thin liquid layer, commonly known as microlayer, beneath itself. This liquid layer subsequently evaporates as the bubble continues to grow. The pool boiling experiments conducted by Moghaddam and Kiger [42] shows that the heat flux spikes during this event by an order of magnitude above the average surface heat flux. As discussed

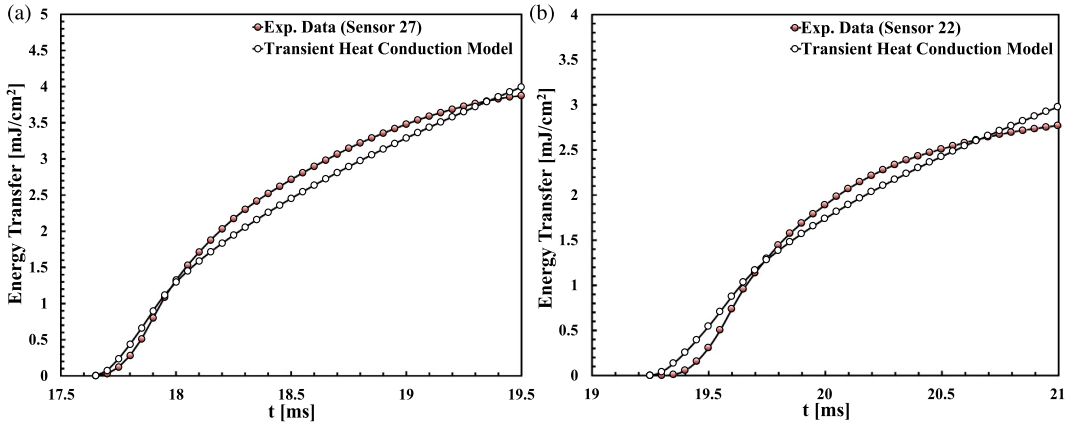


**Fig. 16.** Comparison between experimental and theoretical values of transient conduction heat transfer in (a) low wall superheat test and (b) high wall superheat test.

earlier, a similar thermal behavior is observed here during the microlayer/interline evaporation heat transfer mechanism following the bubble expansion over the heat transfer surface.

2. In the pool boiling process, when the bubble/surface contact area reaches its maximum diameter, the apparent contact line starts to advance and the bubble departure stage begins. The advancing liquid rewets the contact area that has been dried out during the bubble growth. The pool boiling data [42] shows a spike in heat flux within the bubble/surface contact area during the bubble departure step due to the transient heat conduction mechanism. This process has been similarly observed here when the rear end of the elongated bubble advances over the heated surface that has been dried out during the microlayer/interline evaporation mode of heat transfer.
3. Experimental pool boiling data of Moghaddam and Kiger [42] also shows that the cyclic bubble ebullition events generate an almost steady enhanced convective effect around the bubble. The heat transfer associated with this process is referred to as micro-convection heat transfer mechanism. The results of this study suggest an enhanced convective effect with a steady nature on both ends of the moving elongated bubble. However, unlike in the pool boiling process, the heat transfer coefficient associated with this mechanism did not change with surface temperature under the test conditions presented here.

For a more detailed description of the heat transfer events at the bubble-surface interface in the pool boiling process, and comparison (time period of activation, relative magnitude of different mechanisms, etc.) with the data presented here, we refer readers to Moghaddam and Kiger [42,48] and Moghaddam [41].

## 8. Conclusion

The thermal field underneath a moving bubble in microchannel flow boiling of FC-72 was successfully resolved with a spatial resolution of 40–65 μm and a temporal resolution of 50 μs. Analysis of the temperature and heat flux data along with synchronized images of bubbles indicated presence of four active mechanisms of heat transfer as a bubble grows and flows through a microchannel. These mechanisms of heat transfer are (1) microlayer evaporation, (2) interline evaporation, (3) transient conduction, and (4) micro-convection. Details of these mechanisms including their time period of activation and their corresponding surface heat flux and heat transfer coefficient were determined.

The microlayer/interline evaporation mode of heat transfer was found to occur when the front side of the moving bubble moves over a sensor. During this mode of heat transfer, which was observed to be active for about 6–8 ms, the heat flux spiked up to 10–14 W/cm$^2$. Following the initial heat flux spike, the local heat flux declined and surface reached to partial dryout conditions. Towards the end of the partial dryout process, the local heat flux rapidly increased as the rear end of the bubble moved over, and rewetted, the sensors. After the liquid slug fully rewetted the surface, the local heat flux gradually decreased and reached to a steady state value. This sudden spike in the local heat flux during the rewetting process is consistent with what is commonly known as transient conduction mode of heat transfer that results from rewetting of a hot surface with the cooler bulk liquid. Also, the steady enhanced convective heat transfer effect associated with the liquid slugs on both ends of the bubble is referred to as micro-convection heat transfer mechanism.

## Conflict of interest

None declared.

## Acknowledgments

This study was supported by a Grant from the National Science Foundation (NSF) under contract CBET-1403657. Fabrication of the devices was conducted in the Nanoscale Research Facility (NRF) at the University of Florida.

## References

[1] S.V. Garimella, L. Cremaschi, S. Trutassanawin, E.A. Groll, S.V. Garimella, Experimental investigation of a miniature-scale refrigeration system for electronics cooling, IEEE Trans. Compon. Packag. Technol. 29 (2006) 678–687.
[2] R.N. Isfahani, A. Fazeli, S. Bigham, S. Moghaddam, Physics of lithium bromide (LiBr) solution dewatering through vapor venting membranes, Int. J. Multiphase Flow 58 (2014) 27–38.
[3] S. Bigham, D. Yu, D. Chugh, S. Moghaddam, Moving beyond the limits of mass transport in liquid absorbent microfilms through the implementation of surface-induced vortices, Energy 65 (2014) 621–630.
[4] S. Bigham, R. Nasr Isfahani, S. Moghaddam, Direct molecular diffusion and micro-mixing for rapid dewatering of LiBr solution, Appl. Therm. Eng. 64 (2014) 371–375.
[5] I. Mudawar, Two-phase microchannel heat sinks: theory, applications, and limitations, J. Electron. Packag. 133 (2011) 041002.
[6] A. Fazeli, M. Mortazavi, S. Moghaddam, Hierarchical biphilic micro/nanostructures for a new generation phase-change heat sink, Appl. Therm. Eng. 78 (2015) 380–386.
[7] I. Mudawar, Assessment of high-heat-flux thermal management schemes, IEEE Trans. Compon. Packag. Technol. 24 (2001) 122–141.
[8] D.B. Tuckerman, R.F.W. Pease, High-performance heat sinking for VLSI, Electron Device Lett. IEEE 2 (1981) 126–129.
[9] T. Kishimoto, T. Ohsaki, VLSI packaging technique using liquid-cooled channels, IEEE Trans. Compon. Packag. Technol. 9 (1986) 328–335.
[10] J.R. Thome, Boiling in microchannels: a review of experiment and theory, Int. J. Heat Fluid Flow 25 (2004) 128–139.
[11] D. Li, G.S. Wu, W. Wang, Y.D. Wang, D. Liu, D.C. Zhang, et al., Enhancing flow boiling heat transfer in microchannels for thermal management with monolithically-integrated silicon nanowires, Nano Lett. 12 (2012) 3385–3390.
[12] V. Khanikar, I. Mudawar, T. Fisher, Effects of carbon nanotube coating on flow boiling in a micro-channel, Int. J. Heat Mass Transfer 52 (2009) 3805–3817.
[13] A. Koşar, C.-J. Kuo, Y. Peles, Boiling heat transfer in rectangular microchannels with reentrant cavities, Int. J. Heat Mass Transfer 48 (2005) 4867–4886.
[14] S.S. Mehendafe, A.M. Jacob, S.S. Mehendale, R.K. Shah, A.M. Jacobi, Fluid flow and heat transfer at micro- and meso-scales with application to heat exchanger design, Appl. Mech. Rev. 53 (2000) 175–193.
[15] S.G. Kandlikar, History, advances, and challenges in liquid flow and flow boiling heat transfer in microchannels: a critical review, J. Heat Transfer 134 (2012) 034001.
[16] S.G. Kandlikar, Fundamental issues related to flow boiling in minichannels and microchannels, Exp. Therm. Fluid Sci. 26 (2002) 389–407.
[17] A.M. Jacobi, J.R. Thome, Heat transfer model for evaporation of elongated bubble flows in microchannels, J. Heat Transfer 124 (2002) 1131–1136.
[18] T. Harirchian, S.V. Garimella, Flow regime-based modeling of heat transfer and pressure drop in microchannel flow boiling, Int. J. Heat Mass Transfer 55 (2012) 1246–1260.
[19] G.M. Lazarek, S.H. Black, Evaporative heat transfer, pressure drop and critical heat flux in a small vertical tube with R-113, Int. J. Heat Fluid Flow 25 (1982) 945–960.
[20] M.W. Wambsganss, D.M. France, J.A. Jendraejczyk, T.N. Tran, Boiling heat transfer in a horizontal small-diameter tube, J. Heat Transfer 115 (1993) 963–972.
[21] T.N. Tran, M.W. Wambsganss, D.M. France, Small circular- and rectangular-channel boiling with two refrigerants, Int. J. Multiphase Flow 3 (1996) 485–498.
[22] J.R. Baird, Z.Y. Bao, D.F. Fletcher, B.S. Haynes, Local flow boiling heat transfer coefficients in narrow conduits, in: Boil. 2000 Phenom. Eng. Appl. Anchorage Alaska, 30 April. May, 2000, pp. 447–466.
[23] S.G. Kandlikar, P. Balasubramanian, An extension of the flow boiling correlation to transition, laminar, and deep laminar flows in minichannels and microchannels, Heat Transfer Eng. 25 (2004) 86–93.
[24] Y.Y. Yan, T.F. Lin, Evaporation heat transfer and pressure drop of refrigerant R-134a in a small pipe, Int. J. Heat Mass Transfer 41 (1998) 4183–4194.
[25] W. Qu, I. Mudawar, Flow boiling heat transfer in two-phase micro-channel heat sinks––I. Experimental investigation and assessment of correlation methods, Int. J. Heat Mass Transfer 46 (2003) 2755–2771.
[26] M.E. Steinke, S.G. Kandlikar, An experimental investigation of flow boiling characteristics of water in parallel microchannels, J. Heat Transfer 126 (2004) 518–526.
[27] S.M. Kim, I. Mudawar, Consolidated method to predicting pressure drop and heat transfer coefficient for both subcooled and saturated flow boiling in micro-channel heat sinks, Int. J. Heat Mass Transfer 55 (2012) 3720–3731.
[28] J.R. Thome, V. Dupont, A.M. Jacobi, Heat transfer model for evaporation in microchannels. Part I: presentation of the model, Int. J. Heat Mass Transfer 47 (2004) 3375–3385.

[29] W. Qu, I. Mudawar, Flow boiling heat transfer in two-phase micro-channel heat sinks––II. Annular two-phase flow model, Int. J. Heat Mass Transfer 46 (2003) 2773–2784.
[30] S.G. Kandlikar, S. Garimella, D. Li, S. Colin, M.R. King, Heat Transfer and Fluid Flow in Minichannels and Microchannels, Elsevier Ltd, 2006.
[31] J. Buongiorno, D.G. Cahill, C.H. Hidrovo, S. Moghaddam, A.J. Schmidt, L. Shi, Micro- and nanoscale measurement methods for phase change heat transfer on planar and structured surfaces, Nanoscale Microscale Thermophys. Eng. 18 (2014) 270–287.
[32] S.R. Rao, F. Houshmand, Y. Peles, Transient flow boiling heat-transfer measurements in microdomains, Int. J. Heat Mass Transfer 76 (2014) 317–329.
[33] M. Freystein, P. Stephan, C. Kirse, Bubble coalescence and moving contact line evaporation during flow boiling in a single minichannel, in: ASME 2013 11th Int. Conf. Nanochannels, Microchannels, Minichannels, ASME, 2013.
[34] G. Wang, P. Cheng, An experimental study of flow boiling instability in a single microchannel, Int. Commun. Heat Mass Transfer 35 (2008) 1229–1234.
[35] T. Yabuki, O. Nakabeppu, Study on heat transfer mechanism of isolated bubble nucleate boiling with MEMS sensors, in: Proc. Int. Heat Transf. Conf. IHTC14, August 8–13, 2010, Washington DC, USA, 2010, pp. 1–7.
[36] L. Zhang, J. Koo, L. Jiang, M. Asheghi, K.E. Goodson, J.G. Santiago, et al., Measurements and modeling of two-phase flow in microchannels with nearly constant heat flux boundary conditions, J. Microelectromech. Syst. 11 (2002) 12–19.
[37] E. Wagner, P. Stephan, High-resolution measurements at nucleate boiling of pure FC-84 and FC-3284 and its binary mixtures, J. Heat Transfer 131 (2009) 121008.
[38] T. Yabuki, T. Saitoh, O. Nakabeppu, Contribution of microlayer evaporation to bubble growth in pool saturated boiling of water, in: Proc. ASME 2013 11th Int. Conf. Nanochannels, Microchannels, Minichannels, ICNMM2013 June 16–19, 2013, Sapporo, Japan, 2013, pp. 1–6.
[39] F. Demiray, J. Kim, Microscale heat transfer measurements during pool boiling of FC-72: effect of subcooling, Int. J. Heat Mass Transfer 47 (2004) 3257–3268.
[40] J.G. Myers, V.K. Yerramilli, S.W. Hussey, G.F. Yee, J. Kim, Time and space resolved wall temperature and heat flux measurements during nucleate boiling with constant heat flux boundary conditions, Int. J. Heat Mass Transfer 48 (2005) 2429–2442.
[41] S. Moghaddam, Microscale study of nucleation process in boiling of low-surface-tension liquids, University of Maryland, College Park, MD, 2006.
[42] S. Moghaddam, K. Kiger, Physical mechanisms of heat transfer during single bubble nucleate boiling of FC-72 under saturation conditions-I. Experimental investigation, Int. J. Heat Mass Transfer 52 (2009) 1284–1294.
[43] S. Moghaddam, K.T. Kiger, A. Modafe, R. Ghodssi, A novel benzocyclobutene-based device for studying the dynamics of heat transfer during the nucleation process, J. Microelectromech. Syst. 16 (2007) 1355–1366.
[44] V.P. Carey, Liquid–vapor Phase Change Phenomena: An Introduction to the Thermophysics of Vaporization and Condensation Processes in Heat Transfer, Hemisphere Publishing Corporation, 1992.
[45] National Instrument SCXI-1581 User Manual, 2006.
[46] B.B. Mikic, W.M. Rohsenow, A new correlation of pool boiling data including the effect of heating surface characteristics, J. Heat Transfer 91 (1969) 245–250.
[47] H.S. Carslaw, J.C. Jaeger, Conduction of Heat in Solids, Oxford University Press, London, UK, 1959.
[48] S. Moghaddam, K. Kiger, Physical mechanisms of heat transfer during single bubble nucleate boiling of FC-72 under saturation conditions. II: theoretical analysis, Int. J. Heat Mass Transfer 52 (2009) 1295–1303.
[49] S.G. Kandlikar, Similarities and differences between flow boiling in microchannels and pool boiling, Heat Transfer Eng. 31 (2010) 159–167.